ELSEVIER

Mechanics of Materials 31 (1999) 43–61

MECHANICS
OF
MATERIALS

A model for the sintering and coarsening of rows of spherical particles

F. Parhami [a], R.M. McMeeking [b,*], A.C.F. Cocks [c], Z. Suo [d]

[a] Cypress Semiconductor, San Jose, CA 95134, USA
[b] Department of Mechanical and Environmental Engineering, University of California, Santa Barbara, CA 93106, USA
[c] Engineering Department, Leicester University, Leicester, LE1 7RH, UK
[d] Department of Mechanical and Aerospace Engineering, Princeton University, Princeton, NJ 08544, USA

Received 11 November 1997; received in revised form 13 July 1998

Abstract

The formation of interparticle contacts and neck growth by grain boundary and surface diffusion during the sintering of rows of spherical particles is modeled. It is shown that rows of identical particles sinter into a metastable equilibrium configuration whereas rows of particles with different sizes evolve continuously by sintering followed by relatively slow coarsening. During coarsening, smaller particles disappear and larger particles grow. The model is based on a variational principle arising from the governing equations of mass transport on the free surface and grain boundaries. Approximate solutions are found through the use of very simple shapes in which the particles are modeled as truncated spheres and neck formation is represented by a circular disc between particles. Free and pressure assisted sintering of rows of identical and different size particles are studied through this numerical treatment. The effect of initial particle sizes, dihedral angles, diffusivities, and applied compressive forces are investigated. © 1999 Published by Elsevier Science Ltd. All rights reserved.

1. Introduction

Densification of a compact made of identical spherical particles depends on the properties of the powder material and the initial relative density of the compact (i.e. the ratio of current density to the full theoretical density of the material). However, densification is limited by the evolution of contacting particles into equilibrium shapes. This shape is defined by the configuration in which the decrease of surface area is balanced by the increase of grain boundary area so that the total free energy is stationary. On the other hand, real powder particles are not identical in size or shape and the equilibrium can easily be perturbed by coarsening. During coarsening, the total surface area is reduced by the growth of larger particles at the expense of the shrinkage of smaller particles and their eventual disappearance.

The modeling of the formation of interparticle contacts and neck growth between powder particles by grain boundary and surface diffusion has been the subject of study by several authors. Kuczynski (1949), Coble (1958), Ashby (1974) and Swinkels and Ashby (1981) have developed analytical relationships for the size of the interparticle contact radius and the center-to-center approach

---

[*] Corresponding author. E-mail: rmcm@engineering.ucsb.edu.

0167-6636/99/$ – see front matter
PII: S0167-6636(98)00049-0

velocity in terms of geometric variables and material properties. These relationships are based on simplifying assumptions about the geometry of the neck and the particle shape. Furthermore, the models are restricted to the very early stages of sintering when the contact size and the radius of curvature at the neck are very small compared to the particle radius.

Nichols and Mullins (1965), Bross and Exner (1979), Svoboda and Riedel (1995), Zhang and Schneibel (1995) and Bouvard and McMeeking (1996) relaxed the constraint of small contact radius and neck radius of curvature and solved the resulting equations by numerical procedures for realistic particle shapes. This approach provides more accurate solutions for the evolution of particle shape, interparticle contact size and particle shrinkage during sintering. Svoboda and Riedel (1995) also introduced a numerical procedure based on the maximization of the rate of dissipation of Gibbs free energy for a pair of particles through grain boundary and surface diffusion. They provided results for the evolution of interparticle necks between particles of like size. Except for Zhang and Schneibel (1995), none of the above studies predicted the equilibrium shape (Lange and Kellett, 1989) for a pair or a row of identical particles which occurs when small perturbations of geometry produce no change in free energy of the system. Only Zhang and Schneibel (1995) computed the evolution of initially circular prisms into their equilibrium shape. Furthermore, little analysis has been done for particles of unequal size, though recently Pan and Cocks (1995), through a numerical procedure, have introduced a two-dimensional model for the coarsening of a row of nonidentical circular prisms in the absence of applied force.

The aim of the current paper is to use the methodology of Svoboda and Riedel (1995) of energy rate extremization to solve the problem of a row of spherical particles with different sizes subject to free and pressure assisted sintering. The model provides insight into the processes by which aggregates of powder of unequal size densify. In addition, such results will be useful as unit solutions for discrete element network studies (Parhami and McMeeking, 1998) of the macroscopic behavior of powders at high temperature during densification.

In this paper, we develop our formulation for energy rate extremization of a row of particles through a variational principle. Then we use this formulation to simulate the growth of interparticle contact and shrinkage of a row of identical particles. Thereafter, we extend the studies to simulate the growth of interparticle contact between particles of different sizes and thus the coarsening phenomenon.

2. Model formulation

2.1. Variational principle

Consider a row of spherical particles in contact, as shown in Fig. 1(a). At high temperature, atoms travel along the free surfaces and the interparticle contacts to reduce the total free energy of surfaces and interfaces of the system. Energy is dissipated in the process of mass transport, because atoms must be driven over energy barriers during the process of diffusion. For example, on being moved to another interstitial site, an atom dissolved in the lattice must first be raised to a higher energy before descending into the new position. The work done to lift the atom over the barriers is not recovered but rather lost in heat, phonons and other energetic activities. An energy balance between sources and sinks occurs such that it extremizes the functional (Needleman and Rice, 1980; Svoboda and Turek, 1991; Svoboda and Riedel, 1995; Sun et al., 1996)

$$\Pi = \dot{G}_{\rm s} + R_{\rm s}, \tag{1}$$

where $\dot{G}_{\rm s}$ is the rate of change of the free energy of the system and $R_{\rm s}$ is one-half of the rate of energy dissipation.

The dissipation is such that

$$R_{\rm s} = \frac{1}{2}\int\limits_{A_{\rm b}} \frac{1}{\mathscr{D}_{\rm b}} \boldsymbol{j}_{\rm b} \cdot \boldsymbol{j}_{\rm b} \, {\rm d}A_{\rm b} + \frac{1}{2}\int\limits_{A_{\rm s}} \frac{1}{\mathscr{D}_{\rm s}} \boldsymbol{j}_{\rm s} \cdot \boldsymbol{j}_{\rm s} \, {\rm d}A_{\rm s}, \tag{2}$$

where $A_{\rm b}$ and $A_{\rm s}$ are the grain boundary and surface areas respectively, $\boldsymbol{j}_{\rm b}$ and $\boldsymbol{j}_{\rm s}$ are the fluxes of material on the grain boundary and on the free

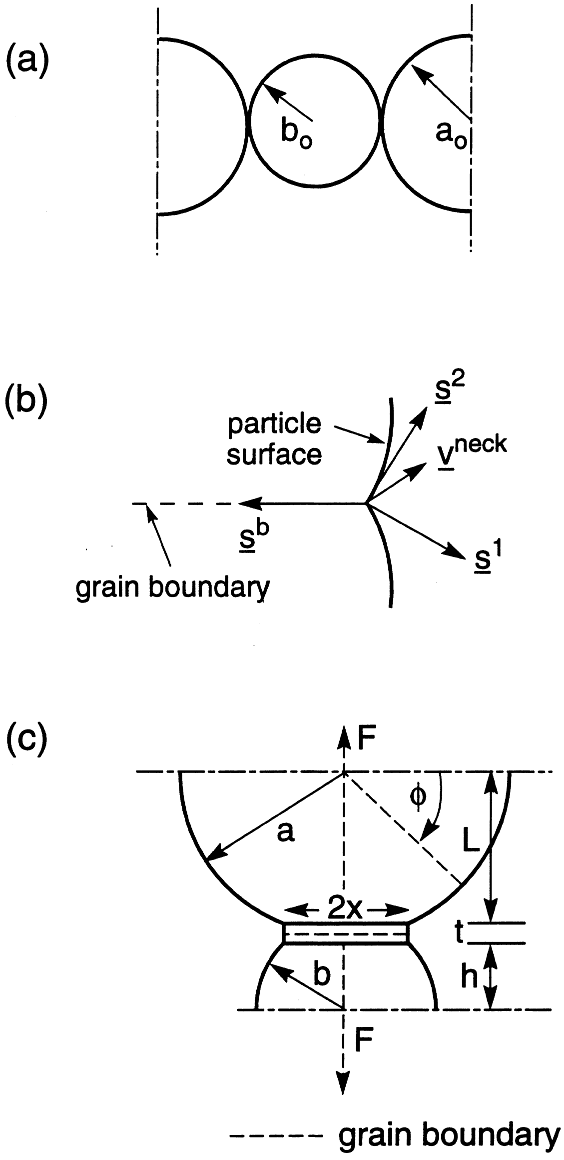

Fig. 1. (a) A row of spherical particles in contact. (b) Representation of unit tangent vectors to the grain boundary and particle surfaces at the neck and the velocity of the neck. (c) A unit problem representing the geometry of a row of particles during neck formation.

surface respectively, $\mathscr{D}_{\mathrm{b}}$ and $\mathscr{D}_{\mathrm{s}}$ are diffusion parameters given by

$$\mathscr{D}_{\mathrm{b}} = \frac{\delta_{\mathrm{b}} D_{\mathrm{b}} \Omega}{kT}, \tag{3}$$

$$\mathscr{D}_{\mathrm{s}} = \frac{\delta_{\mathrm{s}} D_{\mathrm{s}} \Omega}{kT}, \tag{4}$$

where D_{b} and D_{s} are the grain boundary and surface atom diffusivities respectively, δ_{b} and δ_{s} are the thicknesses within which diffusion occurs on the grain boundary and the surface respectively, Ω is the atomic volume, k is Boltzman's constant and T is the absolute temperature. The fluxes $\boldsymbol{j}$ are defined as the volume of material passing by diffusion through unit length in unit time.

The rate of change of the free energy of the system is the rate of change of the internal energy minus the external work rate. In the system under consideration, internal energy is the sum of surface and grain boundary energies. Therefore

$$\dot{G}_{\mathrm{s}} = \gamma_{\mathrm{s}} \dot{A}_{\mathrm{s}} + \gamma_{\mathrm{b}} \dot{A}_{\mathrm{b}} - Fv, \tag{5}$$

where γ_{s} and γ_{b} are the surface and grain boundary energies per unit area respectively, F is the applied force and v is the velocity of one end of the row of particles relative to the other.

It can be demonstrated that the functional Π has a stationary minimum value with respect to compatible variations of $\boldsymbol{j}_{\mathrm{b}}$, $\boldsymbol{j}_{\mathrm{s}}$, $\dot{A}_{\mathrm{s}}$, $\dot{A}_{\mathrm{b}}$ and v, and that this leads to the appropriate governing equations for the mass transport problem on the actual free surface and grain boundary of the row of particles (Needleman and Rice, 1980; Svoboda and Turek, 1991; Svoboda and Riedel, 1995; Sun et al., 1996). This is demonstrated in Appendix A. Consideration of the governing differential equations of the problem is found in Herring (1951), Asaro and Tiller (1972) and Chuang et al. (1979).

2.2. Rayleigh–Ritz method

Since a minimum principle is available, it can be used to obtain approximate solutions to the problem using a Rayleigh–Ritz approach. Simple but robust representations of the evolving shape of the row of particles can be used which depend on only a few parameters of shape. In our calculations, we have used the shape shown in Fig. 1(c) of truncated spheres joined by discs. For a periodic row of particles, this shape depends on only four independent parameters. The grain boundary is in the middle of the disc. (A simpler shape of two truncated barrels without the disc at the contact could be used as invoked by Sun et al. (1996) in their study of evolution of grain shape in cylindrical lines. However, the initial behavior of very small contacts with undercutting is thought to be better represented by the presence of the disc.) The calculations are initiated with the disc absent (i.e. $t = 0$) and the disc is allowed to appear or disappear according to the evolution of the numerical results. The rates of change of the shape parameters become the degrees of freedom of the variational functional Π. However, the rates of change of the shape parameters must preserve compatibility and volume. For the periodic system shown in Fig. 1(a), this will eliminate one parameter so that Π depends finally on three independent degrees of freedom. Minimizations of Π with respect to these three parameters then provides three coupled linear equations for the rates of change of the shape parameters which can be solved to provide values for them. These rates of change of shape parameters are then used for a finite time increment to update the shape of the system. This process is repeated so that the evolution of the shape in time can be computed incrementally. In this way, approximate solutions can be obtained with modest amounts of computation.

Note that the chosen shape in Fig. 1(c) does not conform to the dihedral angle at the neck. In the solution, the dihedral angle at the neck may never be satisfied in the evolution of the simple shapes used in the computation. The variational method, however, produces the best overall shape within the class of shapes permitted by the degrees of freedom employed. Thus, a given local condition such as dihedral angle may not be satisfied but enforced only in the weak variational sense. On the other hand, the vector fields for the fluxes $\boldsymbol{j}_s$ and $\boldsymbol{j}_b$ on the particle surfaces and on the grain boundary must be computed compatibly with the rate of change of shape. The diffusion fluxes on the surface and the contact obey Eqs. (A.4) and (A.5) for the chosen shape and the flux of material at the neck must be equal to the sums of the fluxes on the particle surfaces at the neck (Eq. (A.6)). Furthermore, the periodic system of Fig. 1(a) requires that no material enters or leaves the unit geometry shown in Fig. 1(c); i.e. the surface fluxes at the top and bottom of the unit geometry are zero. This also means that the volume of the unit cell shown in Fig. 1(c) stays constant during the evolution of the shape. These conditions arising from the requirements of compatibility are *essential* conditions in the terminology of variational methods.

A further point is that the chosen shape is capable of representing special configurations, the most notable being when the disc at the contact is absent, i.e. $t = 0$ (see Fig. 2(a) and (c)). The dihedral angle at the neck can then be represented exactly. The feature that in equilibrium, the grain boundary, which is taken to be flat, bisects the dihedral angle is not always satisfied. However, when the two particles are of equal size, all conditions can be met and this occurs in the equilibrium condition depicted in Fig. 2(c). Another special shape which can be represented is a long cylindrical line when the neck disc absorbs the truncated spheres as shown in Fig. 2(b).

We define a unit problem as shown in Fig. 1(c). In this figure, F is the applied force, a and b the radii of the larger and smaller particles respectively, t the thickness of a circular disc between the truncated spheres, representing neck formation, L and h the distances between the circular disc and the center of the larger and smaller particles respectively and x the radius of the circular disc. It is assumed that throughout the process, the initially spherical surfaces remain spherical but their radii may grow or shrink. Similarly, the circular disc may thicken or get thinner and may increase or reduce its radius. The problem is therefore axisymmetric.

The aim of the method is to find the rate of change of the independent degrees of freedom, a, b and x in terms of geometric variables, the applied force, and material properties. The parameters of the model will be given in terms of the response of the unit cell of Fig. 1(c). From the geometry, the relative velocity v^b across the grain boundary is $v^b = \dot{L} + \dot{h} + \dot{t}$. The compatibility condition between the flux and relative velocity, see Eq. (A.5), can then be integrated to give

$$j_\rho = -\frac{\rho}{2}(\dot{L} + \dot{h} + \dot{t}), \tag{6}$$

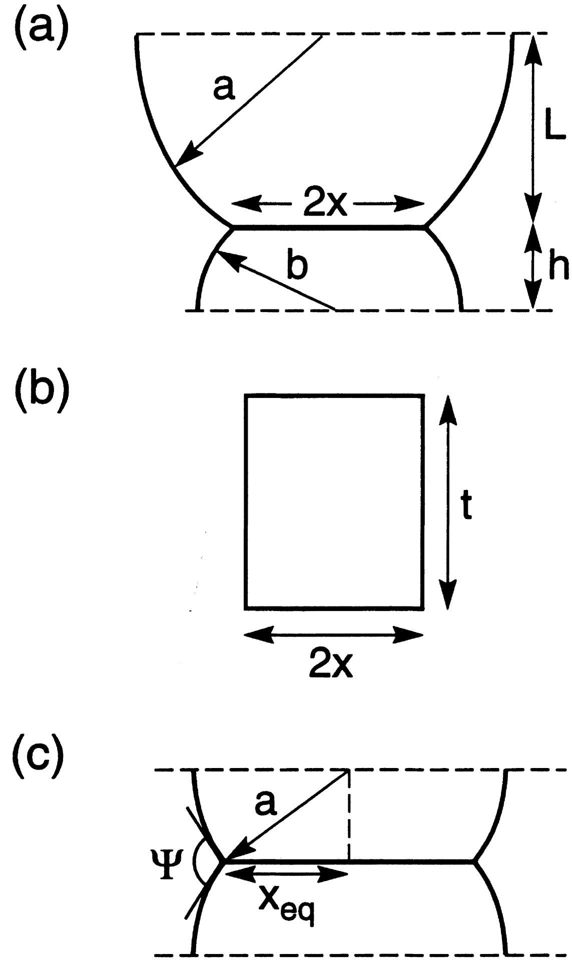

Fig. 2. (a) Configuration resulting from elimination of the circular plate. (b) Configuration resulting from elimination of spherical surfaces. (c) Equilibrium configuration of a row identical spherical particles.

where ρ is the radial distance in the grain boundary from the axis of symmetry and j_ρ, which must be zero at $\rho = 0$, is the radial flux in the grain boundary. Therefore, the virtual dissipation rate in the grain boundary is

$$\int\limits_{A_\mathrm{b}} \frac{1}{\mathscr{D}_\mathrm{b}} \boldsymbol{j}_\mathrm{b} \cdot \delta \boldsymbol{j}_\mathrm{b} \, \mathrm{d}A_\mathrm{b} = 2\pi \int\limits_0^x \frac{\rho}{\mathscr{D}_\mathrm{b}} j_\rho \delta j_\rho \, \mathrm{d}\rho = \frac{\pi x^4}{8\mathscr{D}_\mathrm{b}} (\dot{L} + \dot{h} + \dot{t})(\delta\dot{L} + \delta\dot{h} + \delta\dot{t}). \tag{7}$$

On the surface of the larger particle, the normal velocity $v_\mathrm{n} = \dot{a}$ and Eq. (A.4) becomes

$$\frac{\mathrm{d}j_\phi}{\mathrm{d}\phi} - j_\phi \tan\phi = -\dot{a}a, \tag{8}$$

where ϕ is defined in Fig. 1(c) and j_ϕ is the azimuthal flux on the surface. Subject to $j_\phi = 0$ at $\phi = 0$, integration of Eq. (8) gives

$$j_\phi = -\dot{a}a \tan\phi. \tag{9}$$

Therefore the sum of the variations of the dissipation rate on the surfaces of the small and large particles is

$$\begin{aligned} &\int\limits_{A_\mathrm{spheres}} \frac{1}{\mathscr{D}_\mathrm{s}} \boldsymbol{j}_\mathrm{s} \cdot \delta \boldsymbol{j}_\mathrm{s} \, \mathrm{d}A_\mathrm{s} \\ &= \frac{2\pi a^4}{\mathscr{D}_\mathrm{s}} \int\limits_0^{\arctan L/x} \tan^2\phi \cos\phi \, \mathrm{d}\phi \, \dot{a}\delta\dot{a} \\ &+ \frac{2\pi b^4}{\mathscr{D}_\mathrm{s}} \int\limits_0^{\arctan h/x} \tan^2\phi \cos\phi \, \mathrm{d}\phi \, \dot{b}\delta\dot{b} \\ &= \frac{2\pi}{\mathscr{D}_\mathrm{s}} (a^4 g_a \dot{a}\delta\dot{a} + b^4 g_b \dot{b}\delta\dot{b}), \end{aligned} \tag{10}$$

where g_a and g_b are given by

$$g_a = Ln\left[\frac{a}{x}\left(1 + \sqrt{1 - \left(\frac{x}{a}\right)^2}\right)\right] - \frac{L}{a}, \tag{11}$$

$$g_b = Ln\left[\frac{b}{x}\left(1 + \sqrt{1 - \left(\frac{x}{b}\right)^2}\right)\right] - \frac{h}{b}. \tag{12}$$

On the free surface of the circular disc, Eq. (A.4) gives

$$\frac{\mathrm{d}j_z}{\mathrm{d}z} = -\dot{x}, \tag{13}$$

where z is the direction perpendicular to the grain boundary. The grain boundary is taken to be positioned at $z = 0$. At $z = t/2$, where the disk meets the large truncated sphere, the flux j_z must be equal to $-j_\phi$. At this position $\phi = \arctan L/x$. Integration of (13) for $z > 0$ therefore gives

$$j_z = \dot{a}a\frac{L}{x} - \dot{x}\left(z - \frac{t}{2}\right) \quad (z \geqslant 0). \tag{14}$$

The equivalent result for $z \leqslant 0$ is

$$j_z = \dot{b}b\frac{h}{x} - \dot{x}\left(z + \frac{t}{2}\right) \quad (z \leqslant 0). \tag{15}$$

The values of j_z in Eqs. (14) and (15) generally differ at $z=0$. The difference is equal to the flux away from the grain boundary. Enforcement of this condition will be taken care of below. The virtual dissipation rate on the disc surface is therefore

$$\begin{aligned}\int\limits_{A_{\text{disc}}} \frac{1}{\mathscr{D}_{\text{s}}} \boldsymbol{j}_{\text{s}} \cdot \delta\boldsymbol{j}_{\text{s}} \,\mathrm{d}A_{\text{s}} &= \frac{2\pi x}{\mathscr{D}_{\text{s}}} \int\limits_{0}^{t/2} \left(\frac{\dot{a}aL}{x} + \frac{\dot{x}t}{2} - \dot{x}z \right) \\ &\quad \times \left(\frac{aL\delta\dot{a}}{x} + \frac{t}{2}\delta\dot{x} - z\delta\dot{x} \right) \mathrm{d}z \\ &\quad + \frac{2\pi x}{\mathscr{D}_{\text{s}}} \int\limits_{-t/2}^{0} \left(\frac{\dot{b}bh}{x} - \frac{\dot{x}t}{2} - \dot{x}z \right) \\ &\quad \times \left(\frac{bh\delta\dot{b}}{x} + \frac{t}{2}\delta\dot{x} - z\delta\dot{x} \right) \mathrm{d}z \\ &= \frac{2\pi x}{\mathscr{D}_{\text{s}}} \left(\frac{\dot{a}a^2L^2t}{2x^2} + \frac{\dot{x}aLt^2}{8x} \right) \delta\dot{a} \\ &\quad + \frac{2\pi x}{\mathscr{D}_{\text{s}}} \left(\frac{\dot{b}b^2h^2t}{2x^2} + \frac{\dot{x}bht^2}{8x} \right) \delta\dot{b} \\ &\quad + \frac{2\pi x}{\mathscr{D}_{\text{s}}} \left(\frac{\dot{a}aLt^2}{8x} + \frac{\dot{b}bht^2}{8x} + \frac{\dot{x}t^3}{12} \right) \delta\dot{x}. \end{aligned} \tag{16}$$

It follows that δR_{s} is the sum of Eqs. (7), (10) and (16).

To compute $\delta\dot{G}_{\text{s}}$ we need to express the surface and grain boundary areas in terms of the geometric parameters identified above:

$$A_{\text{s}} = 2\pi aL + 2\pi bh + 2\pi xt \tag{17}$$

and

$$A_{\text{b}} = \pi x^2. \tag{18}$$

Therefore

$$\gamma_{\text{s}}\delta\dot{A}_{\text{s}} = 2\pi\gamma_{\text{s}}(a\delta\dot{L} + L\delta\dot{a} + b\delta\dot{h} + h\delta\dot{b} + x\delta\dot{t} + t\delta\dot{x}) \tag{19}$$

and

$$\gamma_{\text{b}}\delta\dot{A}_{\text{b}} = 2\pi\gamma_{\text{b}}x\delta\dot{x}, \tag{20}$$

whereas

$$F\delta v = F(\delta\dot{L} + \delta\dot{h} + \delta\dot{t}). \tag{21}$$

The result for $\delta\dot{G}_{\text{s}}$ is computed from Eq. (5). The Rayleigh–Ritz minimization is achieved by setting $\delta\Pi = \delta\dot{G}_{\text{s}} + \delta R_{\text{s}} = 0$. Since $\delta\Pi$ must be zero for arbitrary variations of $\delta\dot{a}, \delta\dot{b}, \delta\dot{L}, \delta\dot{h}, \delta\dot{t}$ and $\delta\dot{x}$, the coefficients of these six quantities in $\delta\Pi$ are set to zero. The resulting expressions are coupled linear equations for $\dot{a}, \dot{b}, \dot{L}, \dot{h}, \dot{t}$ and $\dot{x}$ having the form

$$\left[\hat{k}\right]\left\{\dot{\hat{\delta}}\right\} = \left\{\hat{f}\right\}, \tag{22}$$

where $\{\dot{\hat{\delta}}\}$ are the rates of change of the six degrees of freedom. This vector plus the coefficient matrix (termed the viscosity matrix by Sun et al., 1996) and the conjugate force vector are given in Appendix B.

The set of variables used above are not independent. By imposing volume conservation and the geometrical constraints given below, the set can be reduced to three independent parameters. Geometric considerations require

$$L^2 = a^2 - x^2 \tag{23}$$

and

$$h^2 = b^2 - x^2. \tag{24}$$

Volume conservation gives

$$t = \frac{1}{x^2}\left[\frac{V_0}{\pi} - \left(a^2L - \frac{1}{3}L^3\right) - \left(b^2h - \frac{1}{3}h^3\right)\right], \tag{25}$$

where V_0 is the volume of two touching hemispheres representing the initial state as shown in Fig. 1(a). The constraints in incremental form can be written as

$$\left\{\dot{\hat{\delta}}\right\} = [C]\left\{\dot{\delta}\right\}, \tag{26}$$

$$\left\{\dot{\delta}\right\} = \left\{\begin{matrix} \dot{a} \\ \dot{b} \\ \dot{x} \end{matrix}\right\}, \tag{27}$$

where $\dot{a}$, $\dot{b}$ and $\dot{x}$ are the chosen independent degrees of freedom. The constraint matrix $[C]$ is given in Appendix C. With these constraints imposed, the sum of the fluxes determined from Eqs. (14) and (15) at $z=0$ and Eq. (6) at $\rho = x$ equals zero, ensuring that continuity of flux where the grain boundary meets the free surface, Eq. (A.6), is satisfied.

The coupled linear equations for the independent variables are then

$$[k]\{\dot{\delta}\} = \{f\}, \tag{28}$$

where

$$[k] = [C]^{\mathrm{T}}[\hat{k}][C] \tag{29}$$

and

$$\{f\} = [C]^{\mathrm{T}}\{\hat{f}\}. \tag{30}$$

The components of the coefficient matrix $[k]$ and the generalized force $\{f\}$, which drive sintering and coarsening, are given in Appendix D.

3. Numerical Procedures

3.1. Initial formation of interparticle contact

At each increment of time, $\dot{a}, \dot{b}$ and $\dot{x}$ are calculated from Eq. (28) and are used to update a, b and x using Euler integration. The initial conditions are $a = a_0$, $b = b_0$ and $x = 0$. It was found that assigning very small values for the magnitude of x results in instability of the numerical scheme. The following asymptotic approach is used to circumvent this problem.

In the limit where x/a, x/b and t/x are much smaller than 1 and higher order terms in Eq. (28) are neglected, the following formulation results:

$$\dot{x} = \frac{[4\mathscr{D}_{\mathrm{b}} g_a g_b + \mathscr{D}_{\mathrm{s}}(g_a + g_b)](2\gamma_{\mathrm{s}} - \gamma_{\mathrm{b}})}{g_a g_b x t^2} - \frac{4\mathscr{D}_{\mathrm{b}} F}{\pi x^3 t}, \tag{31}$$

$$\dot{a} = -\frac{\mathscr{D}_{\mathrm{s}}(2\gamma_{\mathrm{s}} - \gamma_{\mathrm{b}})}{g_a t a^2} + \frac{t\mathscr{D}_{\mathrm{b}} F}{6\pi x^3 a^2 g_a}, \tag{32}$$

$$\dot{b} = -\frac{\mathscr{D}_{\mathrm{s}}(2\gamma_{\mathrm{s}} - \gamma_{\mathrm{b}})}{g_b t b^2} + \frac{t\mathscr{D}_{\mathrm{b}} F}{6\pi x^3 b^2 g_b}, \tag{33}$$

$$t = \frac{1}{x^2}\left[\frac{V_0}{\pi} - \frac{2}{3}(a^3 + b^3) + \frac{x^4}{4}\left(\frac{1}{a} + \frac{1}{b}\right)\right]. \tag{34}$$

It can be seen from Eqs. (11) and (12) that g_a and g_b are logarithmically divergent when x goes to zero. This could be used to simplify further the expressions in Eqs. (31)–(34). However, the logarithmic singularities are so weak that it is preferable to retain the form as given, except for the first step of the calculation. In this step $1/g_a$ and $1/g_b$ are considered negligible and therefore

$$\dot{x} = \frac{4\mathscr{D}_{\mathrm{b}}(2\gamma_{\mathrm{s}} - \gamma_{\mathrm{b}})}{x t^2} - \frac{4\mathscr{D}_{\mathrm{b}} F}{\pi x^3 t}. \tag{35}$$

When $\dot{a}/\dot{x}$ is computed using Eqs. (32) and (35), it is found that the ratio is always small unless $\mathscr{D}_{\mathrm{b}}$ is negligible. We will always take $\mathscr{D}_{\mathrm{b}}$ to be comparable to $\mathscr{D}_{\mathrm{s}}$, so $\dot{a}/\dot{x}$ can be taken to be zero for the first step. A similar result prevails for $\dot{b}/\dot{x}$, so in the first step of the calculation, $\dot{a} = \dot{b} = 0$ is used. This means that throughout this step, $a = a_0$ and $b = b_0$ and thus Eq. (34) simplifies to

$$t = \frac{x^2}{4}\left(\frac{1}{a_0} + \frac{1}{b_0}\right). \tag{36}$$

Eq. (35) then integrates to give

$$x^6 = 96\mathscr{D}_{\mathrm{b}}\left[\frac{4(2\gamma_{\mathrm{s}} - \gamma_{\mathrm{b}})}{(1/a_0 + 1/b_0)^2} - \frac{F}{\pi(1/a_0 + 1/b_0)}\right]T_{\mathrm{e}}, \tag{37}$$

where T_{e} is the time elapsed since the particles first touched. When $a_0 = b_0$, $F = 0$, and the dihedral angle is 180° ($\gamma_{\mathrm{b}} = 0$), Eq. (37) is Coble's free sintering result (Coble, 1958). Therefore, we can regard Eq. (37) as a generalization of Coble's analysis. Eq. (37) is used to compute x at the end of the first time increment and thereafter Eqs. (31)–(34) are used until x/a reaches a value of 0.01. Eq. (28) is used thereafter with the expressions in Appendix D utilized for the matrix of coefficients and the right-hand side array.

3.2. Elimination of the circular disc

At some point, the numerical simulation reaches a situation where the circular disc (i.e. t) disappears. This configuration usually arises late in the sintering process. The formulation must be adjusted for this case. After the disc disappears, there are two independent variables a and b as shown in Fig. 2(a). Furthermore, since t is zero and remains zero, $\dot{t}$ is also zero. The constraint equations are then

$$\left\{\dot{\hat{\delta}}\right\} = [\overline{C}]\left\{\begin{matrix}\dot{a}\\ \dot{b}\end{matrix}\right\} \tag{38}$$

with $[\overline{C}]$ as given in Appendix E. The governing equations are thus

$$[\overline{k}]\left\{\begin{matrix}\dot{a}\\ \dot{b}\end{matrix}\right\} = \left\{\begin{matrix}\overline{f}_1\\ \overline{f}_2\end{matrix}\right\}, \tag{39}$$

where

$$[\overline{k}] = [\overline{C}]^{\mathrm{T}}\left[\hat{k}\right][\overline{C}] \tag{40}$$

and

$$\left\{\begin{matrix}\overline{f}_1\\ \overline{f}_2\end{matrix}\right\} = [\overline{C}]^{\mathrm{T}}\{\hat{f}\}. \tag{41}$$

When $[\hat{k}]$ and $\{\hat{f}\}$ are evaluated in this case, $t = 0$. The components of $[\overline{k}]$ and $\{\overline{f}\}$ are given in Appendix E. After each increment, Eq. (28) is used to check whether the central disc will grow. If the results show that $\dot{t} \leqslant 0$, the calculations are continued with $t = 0$ using Eq. (39). If $\dot{t} > 0$, the calculations are continued using Eq. (28).

3.3. Elimination of the spherical surfaces

In some cases, the configuration becomes a cylinder due to the circular disc thickening to replace the spherical surfaces which disappear. This configuration is depicted in Fig. 2(b) and results in

$$\dot{x} = \frac{12\mathscr{D}_{\mathrm{s}}\mathscr{D}_{\mathrm{b}}(\pi\gamma_{\mathrm{s}}xt - \pi\gamma_{\mathrm{b}}x^2 - Ft)}{\mathscr{D}_{\mathrm{b}}\pi x^2t^3 + 3\mathscr{D}_{\mathrm{s}}\pi x^3t^2} \tag{42}$$

with

$$t = V_0/\pi x^2, \tag{43}$$

since only Eqs. (7), (16) and (19)–(21) contribute to the result with x and t the only nonzero terms. This configuration is reached when the dihedral angle is large or when large compressive forces are applied. It provides the metastable equilibrium shape for $\gamma_{\mathrm{b}} = 0$. When the original particles are identical, this configuration, as shown in Fig. 2(b), can approximate the equilibrium configuration of Fig. 2(c). When the particles are not initially identical, the cylindrical configuration approximates the coarsened stage after the smaller particle has completely disappeared.

4. Results and discussion

4.1. Free sintering of rows of identical particles

Fig. 3 shows the growth of the interparticle contact radius x vs. time for various dihedral angles and $\mathscr{D}_{\mathrm{b}}/\mathscr{D}_{\mathrm{s}} = 1$. The shape of the unit geometry in the two main stages is shown. Note that somewhere between $x/a_0 = 10^{-1}$ and $x/a_0 = 1$ the circular disc disappears. The dips in our numerical results are associated with this disappearance. The development and disappearance of the circular disc is similar to the development and disappearance of the undercutting at the neck in more exact treatments. The numerical results are somewhat erratic at the beginning, corresponding to the transition from the asymptotic formulation (i.e. Eqs. (31)–(34)) to the full set of equations (i.e. Eq. (28)). This occurs when the neck is so small that the nonsmooth feature of the results here is of no importance.

Also shown in the figure are Coble's analytical solution (Coble, 1958) and the numerical results of Svoboda and Riedel (1995), Zhang and Schneibel (1995) and Bouvard and McMeeking (1996). The Coble solution is as given in Eq. (37) with $b_0 = a_0$, $F = 0$ and $\gamma_{\mathrm{b}} = 0$. It is evident that early in the process our results agree very well with Coble's analytical solution. Later, our results deviate from Coble's solution and reach an equilibrium config-

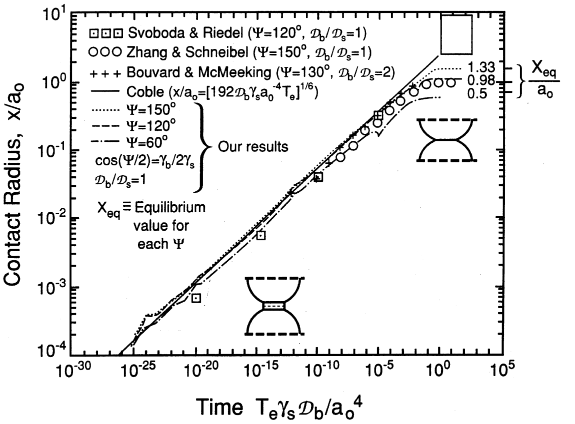

Fig. 3. Contact radius vs. time for the free sintering of a row of identical particles for various dihedral angles.

uration. In this configuration, the driving force in Eq. (39) is zero. By setting $\overline{f}_1$ to zero with $a = b$, $h = L$ and $F = 0$, it is calculated that

$$x = a\ \sin\frac{\Psi}{2}, \tag{44}$$

where it should be recalled that $\gamma_b = 2\gamma_s \cos \psi/2$. The value of x in Eq. (44) is the exact value for the neck radius at equilibrium (Lange and Kellett, 1989) as shown in Fig. 2(c), i.e. x_{eq}. Volume conservation can be used to show that, in terms of the initial particle radius

$$\frac{x_{eq}}{a_0} = \frac{\sin\frac{\Psi}{2}}{\left[\frac{3}{2}\cos\frac{\Psi}{2} - \frac{1}{2}\cos^3\left(\frac{\Psi}{2}\right)\right]^{1/3}}. \tag{45}$$

The relevant results for x_{eq}/a_0 for each dihedral angle are indicated in Fig. 3.

It can be seen that there is good agreement and the simple model results reach the equilibrium configuration. Note that even though Coble's solution (Coble, 1958) is for the case of $\Psi = 180°$, it shows good agreement with our results in the early and intermediate stage of sintering regardless of the dihedral angle. Presumably, this is due to a weak dependence of x on the dihedral angle, as suggested by the asymptotic result of Eq. (37). Only later in the process, and during the evolution of the equilibrium configuration, does the dihedral angle Ψ become important. Our results also show good agreement with the numerical solutions of Svoboda and Riedel (1995) and Bouvard and McMeeking (1996) which are calculated for $\Psi = 120°$ and $\mathscr{D}_b/\mathscr{D}_s = 1$ and $\Psi = 130°$ and $\mathscr{D}_b/\mathscr{D}_s = 2$, respectively. When plotted on a log–log scale as in Fig. 3, it is difficult to discern any difference between the results of Svoboda and Riedel (1995) and Bouvard and McMeeking (1996) despite the differences in dihedral angles and surface diffusion coefficient. The difference between our results and the results of Zhang and Schneibel (1995) calculated for $\Psi = 150°$ and $\mathscr{D}_b/\mathscr{D}_s = 1$ is presumably because their simulation is performed on a pair of prisms in contact and not a row of particles. The discrepancy is most notable in the equilibrium configuration. Thus the agreement with more thorough numerical efforts is remarkable given that our calculations were done with a 3-parameter shape approximation.

Fig. 4 shows the center-to-center distance between neighboring particles for various dihedral angles vs. time. The results have been compared with Coble's prediction (Coble, 1958) and the results of Zhang and Schneibel (1995) and Bouvard and McMeeking (1996). The agreement between our results for $\Psi = 120°$ and those of Bouvard and McMeeking (1996) for $\Psi = 130°$ is very good. As before, it is likely that the difference between our results and those of Zhang and Schneibel (1995) calculated for $\Psi = 150°$ is because their simulation represents the sintering of a pair of prisms and our simulation represents sintering of a row of particles. A result due to Coble (1958) is also shown in Fig. 4. It can be obtained from Eq. (23) with $a = a_o$ and x small compared to a_0. When combined with t from Eq. (36), it gives, to first order, the center-to-center spacing

$$\frac{2L + t}{a_0} = 2 - \frac{1}{2}\left(\frac{x}{a_0}\right)^2. \tag{46}$$

This predicts the shrinkage poorly when it first becomes significant, but it later gives reasonable agreement with our results until equilibrium is approached. The value predicted in our results for the center-to-center distance at the equilibrium configuration is the exact result as calculated according to Fig. 2(c). This gives a prediction of

$$\frac{2L_{eq}}{a_0} = \frac{2\cos\frac{\Psi}{2}}{\left[\frac{3}{2}\cos\frac{\Psi}{2} - \frac{1}{2}\cos^3\left(\frac{\Psi}{2}\right)\right]^{1/3}}, \tag{47}$$

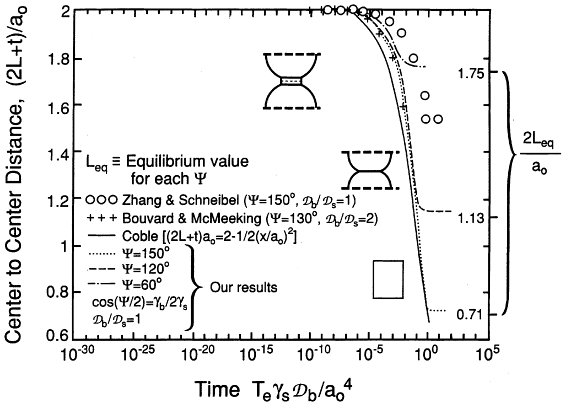

Fig. 4. Center-to-center distance vs. time for the free sintering of a row of particles for various dihedral angles.

which is indicated for each dihedral angle in Fig. 4. Our results compare well with the more exact value shown in Fig. 4.

Fig. 5 shows how the radius of the particle varies with time. This figure shows that initially the particle radius does not change significantly, indicating that during the early stages of sintering, neck formation and shrinkage is mainly dominated by grain boundary diffusion. Surface diffusion, which affects the radius, only becomes important later in the process. The results confirm Coble's assumption (Coble, 1958) that in the early stage the particle radius does not change. This result is consistent with the analysis that led to the result of Eq. (37). The reason for the dip in the plot of particle radius vs. time for $\Psi = 150°$ is that in this case, the growth of the circular disc dominates the later stages of sintering. As the disc grows, both radially and axially, the radius of the spherical region gradually reduces until the radius of the disc, x, equals the particle radius a. This occurs at a radius corresponding to the minimum of Fig. 5. At this point the spherical region disappears and the shape of the particle is represented by a cylinder. In order to complete Fig. 5 we now interpret the radius of the cylinder as the radius of the particle. This radius gradually increases as the particle spreads out radially and reduces in length. Close to the equilibrium configuration the spherical region reforms at the center of the particle and spreads along its length. If we ignore the redevelopment of this spherical region a pseudo equilibrium cylindrical profile is achieved when, $a/a_0 = x/a_0 = 1.37$, which is very close to the true equilibrium value of 1.38 indicated in Fig. 5 determined from

$$\frac{a}{a_0} = \frac{1}{\left[\frac{3}{2}\cos\frac{\Psi}{2} - \frac{1}{2}\cos^3\left(\frac{\Psi}{2}\right)\right]^{1/3}}. \tag{48}$$

The results from the numerical simulation for the particle (or disc) radius in the equilibrium configuration for the other values of Ψ are in exact agreement with the predictions of Eq. (48), which are indicated on Fig. 5.

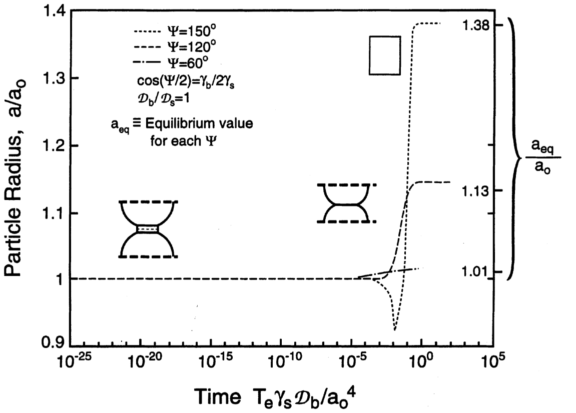

Fig. 5. Particle radius vs. time for the free sintering of a row of identical particles for various dihedral angles.

4.2. Free sintering of rows of different size particles

Fig. 6 shows the variation of the interparticle neck radius between two different size particles with time for different ratios of initial particle radii. These simulations are performed for $\Psi = 120°$ and $\mathscr{D}_b/\mathscr{D}_s = 1$. The shape of the unit geometry in the two main stages is shown. The circular disc disappears somewhere between $x/a_0 = 10^{-1}$ and $x/a_0 = 1$ and the dip in the plot is associated with this disappearance. It can be seen that the interparticle neck radius reaches a maximum level. Until this maximum, the process is dominated by sintering, which causes neck growth. After the maximum, surface diffusion dominates and the coarsening process results in the disappearance of the smaller particle. The calculation was not continued thereafter, but if this had been done, all three cases would have evolved to the equilibrium configuration for the remaining equal sized particles. This is given by

$$\frac{x}{a_0} = \left[\frac{1 + (b_0/a_0)^3}{3\cos\frac{\Psi}{2} - \cos^3\left(\frac{\Psi}{2}\right)}\right]^{1/3} \sin\frac{\Psi}{2}, \tag{49}$$

which indicates that further rearrangement would occur in each case after the small particles disappear.

Also shown in Fig. 6 is Coble's analytical solution (Coble, 1958), as given in Eq. (37) with $a_0 = b_0$, $F = 0$ and $\Psi = 180°$. Our results for $b_0/a_0 = 0.9$ are very close to Coble's prediction showing that initially, neck growth does not depend strongly on the initial ratio of particle radii.

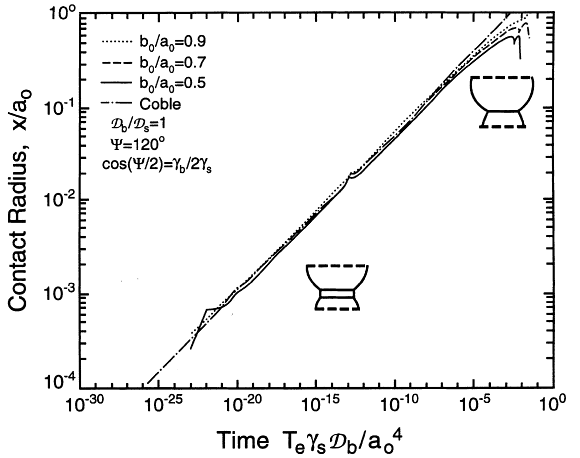

Fig. 6. Contact radius vs. time for the free sintering of a row of particles for various initial size ratios.

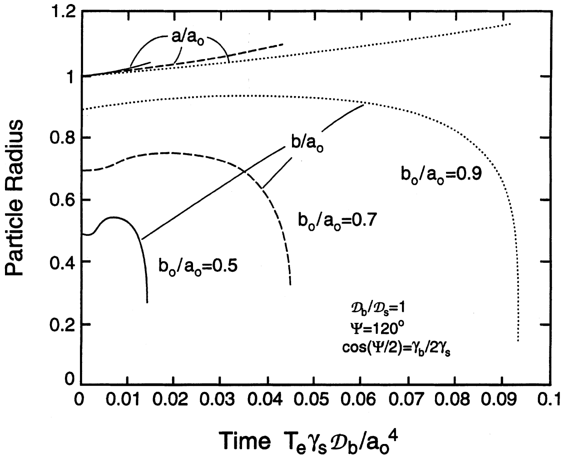

Fig. 7. Particle radii vs. time for the free sintering of a row of particles for various initial size ratios.

Late in the process, however, the radius of the smaller particle influences the neck growth. Decreasing the ratio b_0/a_0 results in a smaller maximum value of x and the earlier disappearance of the smaller particle.

Fig. 7 shows the particle radii vs. time for different initial ratios of particle sizes. Initially, the particle sizes change gradually but later the smaller particle shrinks rapidly and disappears while the larger particle continues to grow gradually. The smaller particle has a finite radius when it vanishes. It is eliminated by the grain boundaries on either side fusing together, i.e. $h \rightarrow 0$. The smaller the second particle the sooner it disappears. Fig. 8 shows how the change in the particles' center-to-center spacing varies with time. Coble's analytical result (Coble, 1958), as given in Eq. (46) for the case $a_0 = b_0$ is shown also. Our simulation for $b_0/a_0 = 0.9$ is similar to, but slower than, Coble's result. Our results indicate that shrinkage is continuous once it becomes significant and occurs during coarsening as well as earlier in sintering. However, the results indicate that diffusional rearrangement of material around the larger particle is the rate controlling mechanism for this process.

Effect of diffusivity ratio: Fig. 9 shows the growth of the interparticle neck radius for an initial size ratio of 0.7, $\Psi = 120°$ and various diffusivity ratios ($\mathscr{D}_b/\mathscr{D}_s$). The figure shows that faster surface diffusivity results in the formation of larger interparticle necks sooner. The results also indicate that the maximum value of x/a_0 is reached earlier and the neck disc is eliminated sooner when $\mathscr{D}_b/\mathscr{D}_s$ is low. This effect is clearer in Fig. 10 where the particle radii are plotted vs. time for various ratios of $\mathscr{D}_b/\mathscr{D}_s$. It can be seen in this figure that the disappearance of the smaller particle occurs sooner when grain boundary diffusion is slow. Fig. 11 is a plot of the particles' center-to-center distance vs. time for various values of $\mathscr{D}_b/\mathscr{D}_s$. This figure shows that shrinkage occurs faster when grain boundary diffusivity is low. In these plots the time has been normalized in terms of the grain-boundary diffusivity. Thus decreasing $\mathscr{D}_b/\mathscr{D}_s$, results in an increase in the rate of surface diffusion, allowing the material to redistribute around the particles quicker. All the above observations are consistent with a net increase in mobility of the material.

Effect of dihedral angle: Fig. 12 shows the growth of the neck radius for an initial size ratio of 0.7 and $\mathscr{D}_b/\mathscr{D}_s = 1$ for various dihedral angles (Ψ). This figure shows that a large dihedral angle results in a high maximum value for the neck radius. When the particle sizes are unequal, a large dihedral angle causes early elimination of the small particles. As before, when $\Psi = 150°$ the growth of the circular disc dominates the process and the spherical surfaces disappear. In this case the evolved shape (a cylinder) is an approximation of

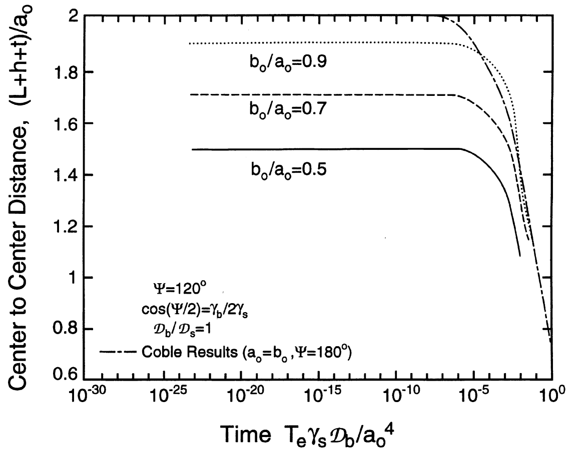

Fig. 8. Center-to-center distance vs. time for the free sintering of a row of particles for various initial size ratios.

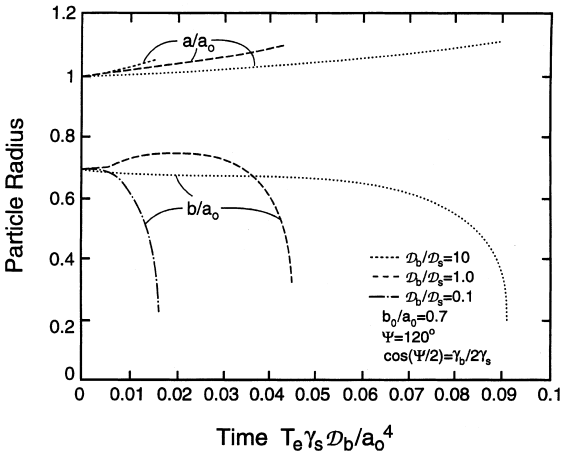

Fig. 10. Effect of grain boundary and surface diffusivity ratio on the free sintering of a row of particles with different sizes. Particle radii vs. time.

the stage where the particles have coarsened and equilibrium of the remaining equal sized particles is reached. In this problem, the total number of particles remains constant, while, for smaller values of Ψ the total number of particles decreases as the larger particles grow at the expense of the smaller ones. This result is a direct consequence of the way in which we have idealized the microstructure. In our formulation of the cylindrical disc, we assume that the grain-boundary is located at the center of the disc. As soon as the second spherical region disappears, the geometry is symmetric and no further transfer of material can occur between the two grains. In practice, coarsening should continue in the same way as is observed for the other values of Ψ considered in Fig. 12. Thus, for $\Psi = 150°$, our idealization overconstrains the evolution process. Additional degrees of freedom are required to more accurately model the system response. This can readily be achieved by replacing the disc by one or two

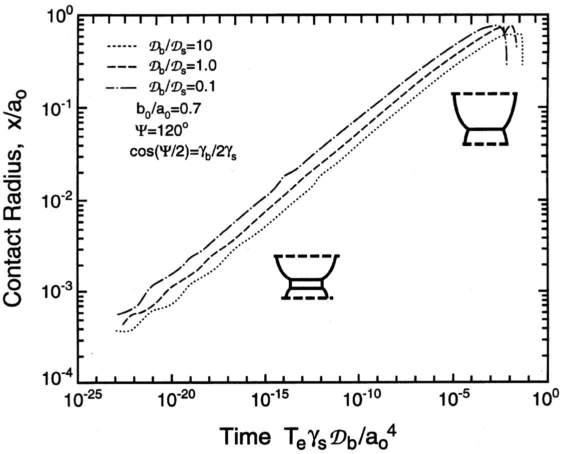

Fig. 9. Effect of grain boundary and surface diffusivity ratio on the free sintering of a row of particles with different sizes. Contact radius vs. time.

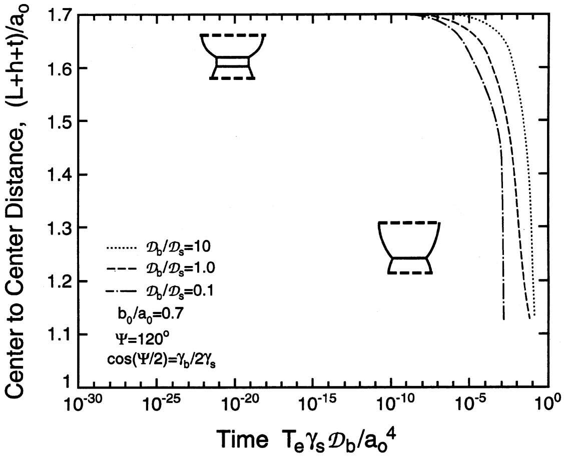

Fig. 11. Effect of grain boundary and surface diffusivity ratio on the free sintering of a row of particles with different sizes. Center-to-center distance vs. time.

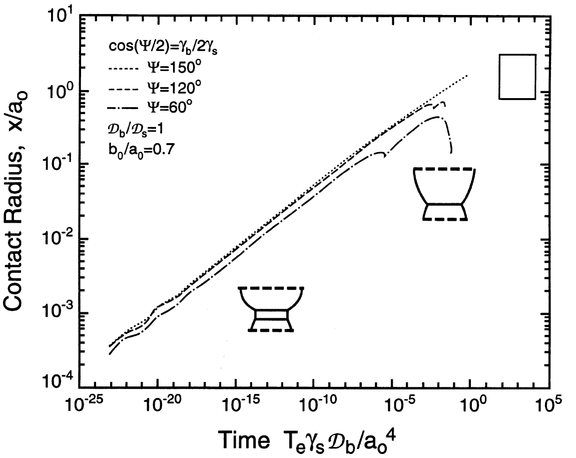

Fig. 12. Contact radius vs. time for the free sintering of a row of particles with an initial size ratio of 0.7 for various dihedral angles.

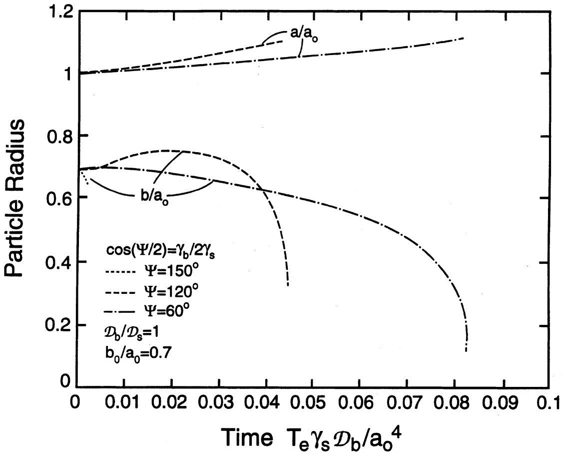

Fig. 13. Particle radii vs. time for the free sintering of a row of particles with an initial size ratio of 0.7 for various dihedral angles.

conical sections. Further consideration of this is beyond the scope of this paper. It is important to note, however, that a sufficient number of degrees of freedom and idealization of the microstructure needs to be adopted to allow the major features of the system response to be modeled. The fewer the degrees of freedom the more thought that must be given to the way in which the microstructure is likely to evolve.

Fig. 13 confirms the results of Fig. 12 by showing that the smaller particle is eliminated earlier as the dihedral angle increases. In fact, the sharp decrease of the neck radius is a consequence of the disappearance of the smaller particle. Fig. 14 shows the influence of the dihedral angle on the way in which the center-to-center distance changes with time. As before, only the early stages of the result for $\Psi = 150°$ can be considered to be reliable.

4.3. Pressure assisted sintering and coarsening

We now consider the influence of a superimposed compressive force on the evolution process. Fig. 15 is a plot of neck radius vs. time for the situation where all the particles are the same size with a dihedral angle of 120°. This figure shows that the application of a compressive force causes the interparticle necks to grow quicker and to eventually achieve a larger final size. For $F/\gamma_s\, a_0 = 0$ and -10 the constrained equilibrium configuration consists of a row of truncated spheres while for $F/\gamma_s\, a_0 = -100$ the final configuration is a row of cylinders. Perturbation of these shapes resulted in no further evolution of microstructure. These shapes therefore represent the minimum energy configurations within the limited class of profiles considered. The value for the contact radius at equilibrium is marked on the figure and can be found by setting the driving force to zero (i.e. setting $\overline{f}_1 = \overline{f}_2 = 0$ in Eqs. (E.12) and (E.13) for the spherical shapes and $\dot{x} = 0$ in Eq. (42) for the cylindrical shape). Fig. 16 shows a plot of the particles' center-to-center distance ($2L + t$) vs. time. The final distance, labeled $2L_{\mathrm{eq}}$ in Fig. 16, is the equilibrium height of the unit cell. This can be computed from volume conservation and the final values for x/a_0 are shown in Fig. 15.

Whereas the magnitudes of our results are sensible for the class of shapes considered, the theoretical equilibrium shape of the particle surfaces under a compressive force are curved, but not spherical. Cannon and Carter (1989) have provided an analysis of the equilibrium shape, although they focus their attention on problems with tension applied rather than compression. The formulae given by Cannon and Carter (1989) are, however, inconsistent with those in the paper by

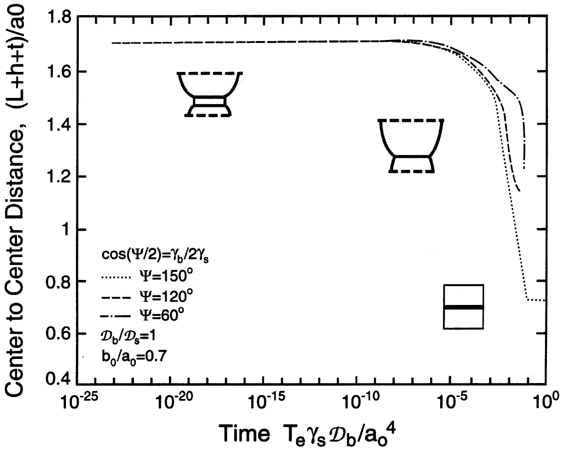

Fig. 14. Center-to-center distance vs. time for the free sintering of a row of particles with an initial size ratio of 0.7 for various dihedral angles.

Carter (1988) serving as a source. After correction to be consistent with Carter (1988) (i.e. in Cannon and Carter (1989) replace sin $\Psi/2$ by $-\cos\Psi/2$ in Eqs. 7(a) and 7(b)), Eq. 7(a) and (8) in Cannon and Carter (1989) can be used to compute parameter values consistent with the compressive forces used to obtain the results in our Figs. 15 and 16. These parameters are then used in their Eq. 7(b) to evaluate L at equilibrium and in their Eq. (6) to give x at equilibrium. The results for $\Psi = 120°$ are $x/a_0 = 1.534$ and $2L_{eq}/a_0 = 0.533$ for $F/\gamma_s a_0 = -10$ and $x/a_0 = 2.583$ and $2L_{eq}/a_0 = 0.197$ for $F/\gamma_s a_0 = -100$. The final neck and particle length shown in Figs. 15 and 16 are within 2% of these exact equilibrium values, thus demonstrating that the simple particle shapes assumed here provide a good approximation of the general features of the evolving microstructure.

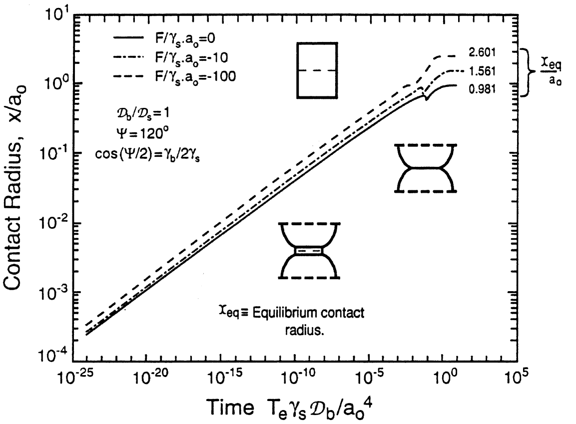

Fig. 15. Effect of compressive force on the sintering of a row of particles with initial size ratio of 0.7. Radius of contact vs. time.

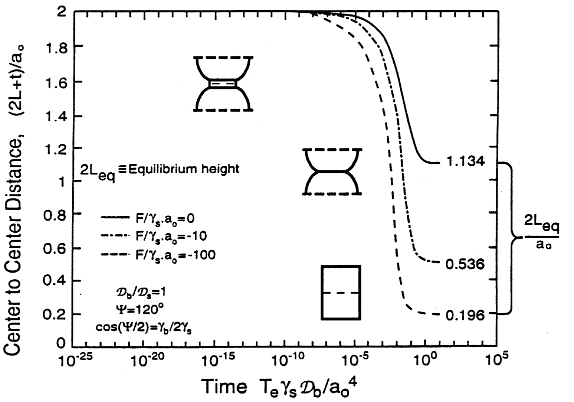

Fig. 16. Effect of compressive force on the sintering of a row of particles with initial size ratio of 0.7. Center-to-center distance vs. time.

In our simulation in which the particles are initially of different radii we find that the central disc dominates the evolution process. As with the free sintering situation considered in Section 4.2 this configuration does not adequately reflect the major features of the microstructure that is likely to evolve. We therefore do not consider this situation further here.

5. Closure

Evolution of identical spherical particles into an equilibrium configuration after sintering is predicted using a simple numerical method. Results show good agreement with Coble's analytical treatment (Coble, 1958) of the problem for early and intermediate configurations. The numerically predicted parameters for the equilibrium shape are in good agreement with the analytical solutions. The simulation also predicts the sintering of different size particles followed by the coarsening process as the large particle absorbs the smaller one. The ratio of initial particle sizes influences the process with a smaller value resulting in a smaller maximum size and an earlier disappearance of the neck. High grain boundary diffusivity results in the later disappearance of the smaller particle and slower shrinkage. A large dihedral angle leads to higher maximum values for the neck radius and the earlier elimination of the smaller particles. The application of a compressive force results in faster neck growth and shrinkage. In addition, a larger neck radius and a smaller center-to-center distance at equilibrium occurs compared to free sintering.

Acknowledgements

This research was supported by NSF Grant DMR 9114560 to the University of California, Santa Barbara.

Appendix A. Weak vs. strong form of the governing equations

The compatibility condition on the rate of change of surface area in Eq. (5) is

$$\dot{A}_\mathrm{s} = \int_{A_\mathrm{s}} \kappa v_\mathrm{n} \mathrm{d}A_\mathrm{s} + \sum_{\text{all b}} \int_{\text{neck}} \boldsymbol{v}^{\text{neck}} \cdot \left(\boldsymbol{s}^1 + \boldsymbol{s}^2\right) \mathrm{d}L, \qquad \text{(A.1)}$$

where κ is the sum of the principal curvatures of the particle surface defined so that positive curvature denotes convexity. The velocity v_n on A_s is the rate of motion of the particle surface in the outward normal direction. The second contribution to $\dot{A}_\mathrm{s}$ in Eq. (A.1) comes from the motion of the locus of points of connection between the grain boundary and free surface of neighboring particles, which can create or destroy surface area. The rate of motion of each point is $\boldsymbol{v}^{\text{neck}}$ and the unit tangent vectors to the surfaces which attach to this point are $\boldsymbol{s}^1$ and $\boldsymbol{s}^2$, as shown in Fig. 1(b). The infinitesimal quantity dL is the length of a line element around the edge of the neck and the integral is taken around the neck. An integral is computed for each grain boundary and summed as indicated where "all *b*" means sum over all grain boundaries.

Similarly, the rate of change of grain boundary area arises from the motion of the neck edge (assuming that the grain boundary is flat or is stationary within the system) and therefore

$$\dot{A}_\mathrm{b} = \sum_{\text{all b}} \int_{\text{neck}} \boldsymbol{v}^{\text{neck}} \cdot \boldsymbol{s}^\mathrm{b} \, \mathrm{d}L, \qquad \text{(A.2)}$$

where $\boldsymbol{s}^\mathrm{b}$ is the tangent unit vector to the grain boundary at the neck, as shown in Fig. 1(b). Given that the particle interior is rigid, the relative velocity v of one end of the row compared to the other is composed of the sum of the relative velocities v^b across all grain boundaries in the row of particles. Furthermore, the force F is equal to the integral of the stress over each grain boundary. Therefore

$$Fv = \sum_{\text{all b}} \int_{A_\mathrm{b}} \sigma \, \mathrm{d}A_\mathrm{b} v^\mathrm{b}. \qquad \text{(A.3)}$$

Compatibility and volume conservation then requires that on A_s

$$v_\mathrm{n} + \boldsymbol{\nabla}^\mathrm{s} \cdot \boldsymbol{j}_\mathrm{s} = 0, \qquad \text{(A.4)}$$

where $\boldsymbol{\nabla}^\mathrm{s}$ is the gradient operator on the particle surface. Similarly, on each grain boundary (which are assumed to be flat)

$$v^\mathrm{b} + \boldsymbol{\nabla}^\mathrm{b} \cdot \boldsymbol{j}_\mathrm{b} = 0, \qquad \text{(A.5)}$$

where $\boldsymbol{\nabla}^\mathrm{b}$ is the gradient operator in the grain boundary. Finally, flux continuity at the necks requires

$$\boldsymbol{s}^1 \cdot \boldsymbol{j}_{\mathrm{s}1} + \boldsymbol{s}^2 \cdot \boldsymbol{j}_{\mathrm{s}2} + \boldsymbol{s}^\mathrm{b} \cdot \boldsymbol{j}_\mathrm{b} = 0, \qquad \text{(A.6)}$$

where $\boldsymbol{j}_{\mathrm{s}1}$ is the flux at the neck on the particle with tangent $\boldsymbol{s}^1$ as shown in Fig. 1(b) and $\boldsymbol{j}_{\mathrm{s}2}$ is the flux at the neck on the particle with tangent $\boldsymbol{s}^2$.

Now let variation of $\boldsymbol{j}_\mathrm{s}$, $\boldsymbol{j}_\mathrm{b}$, $\dot{A}_\mathrm{s}$, $\dot{A}_\mathrm{b}$ and v occur along with variations of v_n, $\boldsymbol{v}^{\text{neck}}$ and v^b, but such that compatibility (Eqs. (A.1)–(A.6)) is obeyed for the varied quantities. It follows that to first order (Needleman and Rice, 1980; Sun et al., 1996)

$$\begin{aligned} \delta\Pi = {} & \Pi\Big(\boldsymbol{j}_\mathrm{s} + \delta\boldsymbol{j}_\mathrm{s}, \boldsymbol{j}_\mathrm{b} + \delta\boldsymbol{j}_\mathrm{b}, \dot{A}_\mathrm{s} + \delta\dot{A}_\mathrm{s}, \dot{A}_\mathrm{b} \\ & + \delta\dot{A}_\mathrm{b}, v + \delta v\Big), \\ & - \Pi\Big(\boldsymbol{j}_\mathrm{s}, \boldsymbol{j}_\mathrm{b}, \dot{A}_\mathrm{s}, \dot{A}_\mathrm{b}, v\Big) = \gamma_\mathrm{s}\delta\dot{A}_\mathrm{s} + \gamma_\mathrm{b}\delta\dot{A}_\mathrm{b} \\ & - F\delta v + \int_{A_\mathrm{b}} \frac{1}{\mathscr{D}_\mathrm{b}} \boldsymbol{j}_\mathrm{b} \cdot \delta\boldsymbol{j}_b \, \mathrm{d}A_\mathrm{b} + \int_{A_s} \frac{1}{\mathscr{D}_\mathrm{s}} \boldsymbol{j}_\mathrm{s} \cdot \delta\boldsymbol{j}_\mathrm{s} \, \mathrm{d}A_\mathrm{s}. \end{aligned} \qquad \text{(A.7)}$$

Use of Eqs. (A.1) and (A.2) in terms of the variations then gives

$$\delta\Pi = \int_{A_s}\left(\gamma_s\kappa\delta v_n + \frac{1}{\mathscr{D}_s}\boldsymbol{j}_s\cdot\delta\boldsymbol{j}_s\right)\mathrm{d}A_s + \sum_{\text{all b}}\int_{\text{neck}}\left[\gamma_s\left(\boldsymbol{s}^1+\boldsymbol{s}^2\right)+\gamma_b\boldsymbol{s}^b\right]\cdot\delta\boldsymbol{v}^{\text{neck}}\,\mathrm{d}L - \sum_{\text{all b}}\int_{A_b}\left(\sigma\delta v^b - \frac{1}{\mathscr{D}_b}\boldsymbol{j}_b\cdot\delta\boldsymbol{j}_b\right)\mathrm{d}A_b. \tag{A.8}$$

Eq. (A.4) is then used to replace δv_n by $-\nabla^s\,.\,\delta\boldsymbol{j}_s$ and Eq. (A.5) allows δv^b to be replaced by $-\nabla^b\,.\,\delta\boldsymbol{j}_b$. This permits $\delta\Pi$ to be restated as

$$\delta\Pi = -\int_{A_s}\left[\gamma_s\nabla^s\cdot(\kappa\delta\boldsymbol{j}_b) - \left(\gamma_s\nabla^s\kappa + \frac{1}{\mathscr{D}_s}\boldsymbol{j}_s\right)\cdot\delta\boldsymbol{j}_s\right]\mathrm{d}A_s + \sum_{\text{all b}}\int_{\text{neck}}\left[\gamma_s\left(\boldsymbol{s}^1+\boldsymbol{s}^2\right)+\gamma_b\boldsymbol{s}^b\right]\cdot\delta\boldsymbol{v}^{\text{neck}}\,\mathrm{d}L + \sum_{\text{all b}}\int_{A_b}\left[\nabla^b\cdot(\sigma\delta\boldsymbol{j}_b) + \left(\frac{1}{\mathscr{D}_b}\boldsymbol{j}_b - \nabla^b\sigma\right).\,\delta\boldsymbol{j}_b\right]\mathrm{d}A_b. \tag{A.9}$$

Use of the divergence theorem on A_s and on A_b then provides

$$\delta\Pi = \sum_{\text{all b}}\int_{\text{neck}}\left[\gamma_s\left(\kappa_1\boldsymbol{s}^1\cdot\delta\boldsymbol{j}_{s1} + \kappa_2\boldsymbol{s}^2\cdot\delta\boldsymbol{j}_{s2} - \sigma\boldsymbol{s}^b\cdot\delta\boldsymbol{j}_b\right)\right]\mathrm{d}L + \int_{A_s}\left(\gamma_s\nabla^s\kappa + \frac{1}{\mathscr{D}_s}\boldsymbol{j}_s\right)\cdot\delta\boldsymbol{j}_s\,\mathrm{d}A_s + \sum_{\text{all b}}\int_{\text{neck}}\left[\gamma_s\left(\boldsymbol{s}^1+\boldsymbol{s}^2\right)+\gamma_b\boldsymbol{s}^b\right]\cdot\delta\boldsymbol{v}^{\text{neck}}\,\mathrm{d}L + \sum_{\text{all b}}\int_{A_b}\left(\frac{1}{\mathscr{D}_b}\boldsymbol{j}_b - \nabla^b\sigma\right)\cdot\delta\boldsymbol{j}_b\,\mathrm{d}A_b, \tag{A.10}$$

where the subscripts on κ denote the different particles meeting at L. Finally, use of Eq. (A.6) gives

$$\delta\Pi = \sum_{\text{all b}}\int_{\text{neck}}\left[(\gamma_s\kappa_1-\sigma)\boldsymbol{s}^1\cdot\delta\boldsymbol{j}_{s1} + (\gamma_s\kappa_2-\sigma)\boldsymbol{s}^2\cdot\delta\boldsymbol{j}_{s2}\right]\mathrm{d}L + \sum_{\text{all b}}\int_{\text{neck}}\left[\gamma_s\left(\boldsymbol{s}^1+\boldsymbol{s}^2\right)+\gamma_b\boldsymbol{s}^b\right]\cdot\delta\boldsymbol{v}^{\text{neck}}\,\mathrm{d}L + \int_{A_s}\left(\gamma_s\nabla^s\kappa + \frac{1}{\mathscr{D}_s}\boldsymbol{j}_s\right)\cdot\delta\boldsymbol{j}_s\,\mathrm{d}A_s + \sum_{\text{all b}}\int_{A_b}\left(\frac{1}{\mathscr{D}_b}\boldsymbol{j}_b - \nabla^b\sigma\right)\cdot\delta\boldsymbol{j}_b\,\mathrm{d}A_b. \tag{A.11}$$

This shows that for arbitrary compatible variations from the problem solution, $\delta\Pi$ is zero. This is true because the pointwise governing equations (Herring, 1951; Asaro and Tiller, 1972; Chuang et al., 1979) are: the flux conditions on the free surface and grain boundaries,

$$\boldsymbol{j}_s = -\mathscr{D}_s\gamma_s\nabla^s\kappa \quad \text{on } A_s, \tag{A.12}$$

$$\boldsymbol{j}_b = \mathscr{D}_b\nabla^b\sigma \quad \text{on } A_b \tag{A.13}$$

the continuity of chemical potential at all junctions between particle surface and grain boundary,

$$\gamma_s\kappa_1 = \gamma_s\kappa_2 = -\sigma \quad \text{on } L \tag{A.14}$$

and the dihedral angle is enforced at the neck,

$$\gamma_s\left(\boldsymbol{s}^1+\boldsymbol{s}^2\right)+\gamma_b\boldsymbol{s}^b = 0 \quad \text{on } L. \tag{A.15}$$

(The latter can only be true if $\boldsymbol{s}^b$ bisects the angle between $\boldsymbol{s}^1$ and $\boldsymbol{s}^2$ and this angle is the dihedral $\Psi = 2\arccos(\gamma_b/2\gamma_s)$). The conditions represented by Eqs. (A.14) and (A.15) are enforced by extremely rapid local motion of material, so that even if an initial shape does not satisfy these equations instantaneously, mass transport enforces them locally. Thereafter, the shape evolutions occurs with Eqs. (A.14) and (A.15) satisfied.

It is also readily shown that the functional Π is minimized. Let the exact solution of the problem be denoted by, $\boldsymbol{j}_{\mathrm{s}}$, $\boldsymbol{j}_{\mathrm{b}}$, $\dot{A}_{\mathrm{s}}$, $\dot{A}_{\mathrm{b}}$ and v. Since the functional Π is stationary for these values,

$$\Pi\left(\boldsymbol{j}_{\mathrm{s}} + \delta\boldsymbol{j}_{\mathrm{s}}, \boldsymbol{j}_{\mathrm{b}} + \delta\boldsymbol{j}_{\mathrm{b}}, \dot{A}_{\mathrm{s}} + \delta\dot{A}_{\mathrm{s}}, \dot{A}_{\mathrm{b}} + \delta\dot{A}_{\mathrm{b}}, v+\delta v\right) - \Pi\left(\boldsymbol{j}_{\mathrm{s}}, \boldsymbol{j}_{\mathrm{b}}, \dot{A}_{\mathrm{s}}, \dot{A}_{\mathrm{b}}, v\right) + \frac{1}{2}\int_{A_{\mathrm{b}}} \frac{1}{\mathscr{D}_{\mathrm{b}}} \delta\boldsymbol{j}_{\mathrm{b}} \cdot \delta\boldsymbol{j}_{\mathrm{b}}\, \mathrm{d}A_{\mathrm{b}} + \frac{1}{2}\int_{A_{\mathrm{s}}} \frac{1}{\mathscr{D}_{\mathrm{s}}} \delta\boldsymbol{j}_{\mathrm{s}} \cdot \delta\boldsymbol{j}_{\mathrm{s}}\, \mathrm{d}A_{\mathrm{s}} \qquad \text{(A.16)}$$

to second order. Since $\mathscr{D}_{\mathrm{s}}$ and $\mathscr{D}_{\mathrm{b}}$ are both positive, the right-hand side is always greater than or equal to zero and therefore Π is minimized by the exact solution.

Appendix B. Governing equations for a row of bidiametrical spheres in terms of six degrees of freedom

The governing equations for the six degrees of freedom $\dot{a}$, $\dot{b}$, $\dot{L}$, $\dot{h}$, $\dot{t}$ and $\dot{x}$ can be stated in matrix form as

$$\left[\hat{k}\right]\left\{\dot{\hat{\delta}}\right\} = \left\{\hat{f}\right\}, \qquad \text{(B.1)}$$

where

$$\left\{\dot{\hat{\delta}}\right\} = \begin{Bmatrix} \dot{a} \\ \dot{b} \\ \dot{L} \\ \dot{h} \\ \dot{t} \\ \dot{x} \end{Bmatrix} \qquad \text{(B.2)}$$

and

$$\left\{\hat{f}\right\} = \begin{Bmatrix} -2\pi\gamma_{\mathrm{s}}L \\ -2\pi\gamma_{\mathrm{s}}h \\ -2\pi\gamma_{\mathrm{s}}a + F \\ -2\pi\gamma_{\mathrm{s}}b + F \\ -2\pi\gamma_{\mathrm{s}}x + F \\ -2\pi\gamma_{\mathrm{s}}t - 2\pi\gamma_{\mathrm{b}}x \end{Bmatrix}. \qquad \text{(B.3)}$$

The nonzero entries in the coefficient matrix are

$$\hat{k}_{11} = \frac{\pi a^2}{x\mathscr{D}_{\mathrm{s}}}\left(2xa^2 g_a + L^2 t\right), \qquad \text{(B.4)}$$

$$\hat{k}_{16} = \frac{\pi a L t^2}{4\mathscr{D}_{\mathrm{s}}}, \qquad \text{(B.5)}$$

$$\hat{k}_{22} = \frac{\pi b^2}{x\mathscr{D}_{\mathrm{s}}}\left(2xb^2 g_b + h^2 t\right), \qquad \text{(B.6)}$$

$$\hat{k}_{26} = \frac{\pi b h t^2}{4\mathscr{D}_{\mathrm{s}}}, \qquad \text{(B.7)}$$

$$\hat{k}_{33} = \hat{k}_{34} = \hat{k}_{35} = \hat{k}_{43} = \hat{k}_{44} = \hat{k}_{45} = \hat{k}_{53} = \hat{k}_{54} = \hat{k}_{55} = \frac{\pi x^4}{8\mathscr{D}_{\mathrm{b}}}, \qquad \text{(B.8)}$$

$$\hat{k}_{61} = \frac{\pi a L t^2}{4\mathscr{D}_{\mathrm{s}}}, \qquad \text{(B.9)}$$

$$\hat{k}_{62} = \frac{\pi b h t^2}{4\mathscr{D}_{\mathrm{s}}}, \qquad \text{(B.10)}$$

$$\hat{k}_{66} = \frac{\pi x t^3}{6\mathscr{D}_{\mathrm{s}}}. \qquad \text{(B.11)}$$

Appendix C. Constraint equations to reduce six degrees of freedom to three independent parameters

With $\left\{\dot{\hat{\delta}}\right\}$ defined as in Appendix A, the constraint equations are

$$\left\{\dot{\hat{\delta}}\right\} = [C]\begin{Bmatrix} \dot{a} \\ \dot{b} \\ \dot{x} \end{Bmatrix} \qquad \text{(C.1)}$$

with the nonzero terms of $[C]$ as follows:

$$C_{11} = C_{22} = C_{66} = 1, \qquad \text{(C.2)}$$

$$C_{31} = \frac{a}{L}, \qquad \text{(C.3)}$$

$$C_{33} = C_{43} = -\frac{x}{L}, \qquad \text{(C.4)}$$

$$C_{42} = \frac{b}{L}, \qquad \text{(C.5)}$$

$$C_{51} = -\frac{2aL}{x^2} - \frac{a}{L}, \qquad \text{(C.6)}$$

$$C_{52} = -\frac{2bh}{x^2} - \frac{b}{h}, \qquad \text{(C.7)}$$

$$C_{53} = \frac{x}{L} + \frac{x}{h} - \frac{2t}{x}. \tag{C.8}$$

Appendix D. Governing equations in terms of three independent degrees of freedom

The symmetric coefficient matrix for Eq. (28) is given by

$$k_{11} = a^2L^2\left(\frac{t}{x\mathscr{D}_\mathrm{s}} + \frac{1}{2\mathscr{D}_\mathrm{b}}\right) + \frac{2}{\mathscr{D}_\mathrm{s}}a^4 g_a, \tag{D.1}$$

$$k_{12} = k_{21} = \frac{aLbh}{2\mathscr{D}_\mathrm{b}}, \tag{D.2}$$

$$k_{13} = k_{31} = aLxt\left(\frac{1}{2\mathscr{D}_\mathrm{b}} + \frac{t}{4x\mathscr{D}_\mathrm{s}}\right), \tag{D.3}$$

$$k_{22} = b^2h^2\left(\frac{1}{2\mathscr{D}_\mathrm{b}} + \frac{t}{x\mathscr{D}_\mathrm{s}}\right) + \frac{2}{\mathscr{D}_\mathrm{s}}b^4 g_b, \tag{D.4}$$

$$k_{23} = k_{32} = bhxt\left(\frac{1}{2\mathscr{D}_\mathrm{b}} + \frac{t}{4x\mathscr{D}_\mathrm{s}}\right), \tag{D.5}$$

$$k_{33} = \frac{x^2t^2}{2}\left(\frac{1}{\mathscr{D}_\mathrm{b}} + \frac{t}{3x\mathscr{D}_\mathrm{s}}\right) \tag{D.6}$$

with Eqs. (27) and (28) repeated for convenience as

$$g_a = Ln\left[\frac{a}{x}\left(1 + \sqrt{1 - \left(\frac{x}{a}\right)^2}\right)\right] - \frac{L}{a}, \tag{D.7}$$

$$g_b = Ln\left[\frac{b}{x}\left(1 + \sqrt{1 - \left(\frac{x}{b}\right)^2}\right)\right] - \frac{h}{b}, \tag{D.8}$$

The generalized force vector is given by

$$f_1 = \frac{4\gamma_\mathrm{s}aL}{x}\left[1 - \frac{x}{2a} - \frac{xa}{2L^2} + \frac{x^2}{2L^2}\right] - \frac{2aL}{\pi x^2}F, \tag{D.9}$$

$$f_2 = \frac{4\gamma_\mathrm{s}bh}{x}\left[1 - \frac{x}{2b} - \frac{xb}{2h^2} + \frac{x^2}{2h^2}\right] - \frac{2bh}{\pi x^2}F, \tag{D.10}$$

$$f_3 = 2\gamma_\mathrm{s}x\left[\frac{a}{L} + \frac{b}{h} - \frac{x}{L} - \frac{x}{h} + \frac{t}{x}\right] - 2\gamma_\mathrm{b}x - \frac{2t}{\pi x}F. \tag{D.11}$$

Appendix E. Constraint matrix after the circular disc has vanished reducing six degrees of freedom to two independent parameters

With $\left\{\dot{\hat{\delta}}\right\}$ defined as in Appendix B, the constraint equations are

$$\left\{\dot{\hat{\delta}}\right\} = [\overline{C}]\begin{Bmatrix}\dot{a}\\ \dot{b}\end{Bmatrix} \tag{E.1}$$

with the nonzero terms of $[\overline{C}]$ as follows:

$$C_{11} = C_{22} = 1, \tag{E.2}$$

$$C_{31} = \frac{a(x^2 - 2hL)}{x^2(h+L)}, \tag{E.3}$$

$$C_{32} = -\frac{b(b^2 + h^2)}{x^2(h+L)}, \tag{E.4}$$

$$C_{41} = -\frac{a(a^2 + L^2)}{x^2(h+L)}, \tag{E.5}$$

$$C_{42} = \frac{b(x^2 - 2hL)}{x^2(h+L)}, \tag{E.6}$$

$$C_{61} = \frac{ah(a^2 + L^2)}{x^3(h+L)}, \tag{E.7}$$

$$C_{62} = \frac{bL(b^2 + h^2)}{x^3(h+L)}. \tag{E.8}$$

The symmetric matrix $[\overline{k}]$ for Eq. (39) is then

$$\overline{k}_{11} = \frac{2\pi a^4 g_a}{\mathscr{D}_\mathrm{s}} + \frac{\pi a^2L^2}{2\mathscr{D}_\mathrm{b}}, \tag{E.9}$$

$$\overline{k}_{12} = \overline{k}_{21} = \frac{\pi abLh}{2\mathscr{D}_\mathrm{b}}, \tag{E.10}$$

$$\overline{k}_{22} = \frac{2\pi b^4 g_b}{\mathscr{D}_\mathrm{s}} + \frac{\pi b^2h^2}{2\mathscr{D}_\mathrm{b}}. \tag{E.11}$$

and the generalized force vector for Eq. (39) is

$$\begin{aligned}\overline{f}_1 = {} & -\frac{2FaL}{x^2} - 2\pi\gamma_\mathrm{b}\frac{ah(a^2 + L^2)}{x^2(h+L)} - 2\pi\gamma_\mathrm{s}L \\ & -\frac{2\pi\gamma_\mathrm{s}a}{x^2(h+L)}\left[a\left(x^2 - 2hL\right) - b\left(a^2 + L^2\right)\right],\end{aligned} \tag{E.12}$$

$$\overline{f}_2 = -\frac{2Fbh}{x^2} - 2\pi\gamma_{\mathrm{b}}\frac{bL(b^2+h^2)}{x^2(h+L)} - 2\pi\gamma_{\mathrm{s}}h - \frac{2\pi\gamma_{\mathrm{s}}b}{x^2(h+L)}\left[b\left(x^2-2hL\right)-a\left(b^2+h^2\right)\right]. \quad \text{(E.13)}$$

References

Asaro, R.J., Tiller, W.A., 1972. Metallurgical Transactions 3, 1789.

Ashby, M.F., 1974. A first report on sintering diagrams. Acta Metallurgica 22, 275.

Bouvard, D., McMeeking, R.M., 1996. The deformation of interparticle necks by diffusion controlled creep. Journal of the American Ceramic Society 79, 666.

Bross, P., Exner, H.E., 1979. Computer simulation of sintering processes. Acta Metallurgica 27, 1013.

Cannon, R.M., Carter, W.C., 1989. Interplay of sintering microstructures, driving forces and mass transport mechanisms. Journal of the American Ceramic Society 72, 1550.

Carter, W.C., 1988. The forces and behavior of fluids constrained by solids. Acta Metallurgica 36, 2283.

Chuang, T.-J., Kagawa, K.I., Rice, J.R., Sills, L.B., 1979. Non-equilibrium models for diffusive cavitation of grain interfaces. Acta Metallurgica 27, 265.

Coble, R.L., 1958. Initial sintering of alumina and hematite. Journal of the American Ceramic Society 41, 55.

Herring, C., 1951. In: Kingston, W.E. (Ed.), Symposium on the Physics of Powder Metallurgy. McGraw-Hill, New York, pp. 143–179.

Kuczynski, G.C., 1949. Self-diffusion in sintering of metallic particles. Transactions of the American Institute of Mining and Metallurgical Engineers 135, 169.

Lange, F.F., Kellett, B.J., 1989. Thermodynamics of densification: II, Grain growth in porous compacts and relation to densification. Journal of the American Ceramic Society 72, 735.

Needleman, A., Rice, J.R., 1980. Plastic creep flow effects in the diffusive cavitation of grain boundaries. Acta Metallurgica 28, 1315.

Nichols, F.A., Mullins, W.W., 1965. Morphological changes of a surface of revolution due to capillarity-induced surface diffusion. Journal of Applied Physics 36, 1826.

Pan, J., Cocks, A.C.F., 1995. A numerical technique for the analysis of coupled surface and grain-boundary diffusion. Acta Metallurgica et Materialia 43, 1395.

Parhami, F., McMeeking, R.M., 1998. A network model of initial stage sintering. Mechanics of Materials 27, 111.

Sun, B., Suo, Z., Cocks, A.C.F., 1996. A global analysis of structural evolution in a row of grains. Journal of the Mechanics and Physics of Solids 44, 559.

Svoboda, J., Riedel, H., 1995. New solutions describing the formation of interparticle necks in solid-state sintering. Acta Metallurgica et Materialia 43, 1.

Svoboda, J., Turek, I., 1991. On diffusion-controlled evolution of closed solid-state thermodynamic systems at constant temperature and pressure. Philosophical Magazine B 64, 749.

Swinkels, F.B., Ashby, M.F., 1981. A second report on sintering diagrams. Acta Metallurgica 29, 259.

Zhang, W., Schneibel, J.H., 1995. The sintering of two particles by surface and grain boundary diffusion-a two dimensional numerical study. Acta Metallurgica et Materialia 43, 4377.